


# Electronic Structure

OPEN ACCESS



TECHNICAL NOTE

## All-electron full-potential implementation of real-time TDDFT in `exciting`

RECEIVED  
8 February 2021REVISED  
26 May 2021ACCEPTED FOR PUBLICATION  
17 June 2021PUBLISHED  
9 July 2021Ronaldo Rodrigues Pela<sup>1,2,\*</sup>  and Claudia Draxl<sup>1,2</sup> <sup>1</sup> Physics Department and IRIS Adlershof, Humboldt-Universität zu Berlin, Zum Großen Windkanal 2, 12489 Berlin, Germany<sup>2</sup> European Theoretical Spectroscopy Facility (ETSF)

\* Author to whom any correspondence should be addressed.

E-mail: [ronaldo@physik-hu.berlin.de](mailto:ronaldo@physik-hu.berlin.de)**Keywords:** time-dependent density functional theory, pump–probe spectroscopy, third harmonic generation, dynamic behavior of excitations

Original content from this work may be used under the terms of the [Creative Commons Attribution 4.0 licence](https://creativecommons.org/licenses/by/4.0/).

Any further distribution of this work must maintain attribution to the author(s) and the title of the work, journal citation and DOI.



### Abstract

Linearized augmented planewaves combined with local-orbitals (LAPW + lo) are arguably the most precise basis set to represent Kohn–Sham states. When employed within real-time time-dependent density functional theory (RT-TDDFT), they promise ultimate precision achievable for exploring the evolution of electronic excitations. In this work, we present an implementation of RT-TDDFT in the full-potential LAPW + lo code `exciting`. We benchmark our results against those obtained by linear-response TDDFT with `exciting` and by RT-TDDFT calculations with the Octopus code, finding a satisfactory level of agreement. To illustrate possible applications of our implementation, we have chosen three examples: the dynamic behavior of excitations in MoS<sub>2</sub> induced by a laser pulse, the third harmonic generation in silicon, and a pump–probe experiment in diamond. Besides, we provide further benchmark results.

## 1. Introduction

TDDFT is a powerful tool to study excitations in many-body systems [1]. It is formally an exact theory that guarantees the existence of a one-to-one mapping between the evolution of the many-body wavefunction and a much less complicated object, namely the time-dependent density [1, 2]. Compared to many-body perturbation theory based on Green functions, TDDFT is computationally less demanding, which allows for studying systems containing up to hundreds or even thousands of atoms [3–7].

In practical problems, TDDFT is usually employed either in the linear-response (LR) regime, where the density is evaluated in the frequency domain as a first-order response to an external perturbation potential, or directly in the time domain, by evolving the Kohn–Sham (KS) wavefunctions [5]. Both approaches have advantages and limitations. Here, we focus on real-time time-dependent density functional theory (RT-TDDFT) that allows, among others, for assessing the nonlinear regime, for studying the dynamics of excitations in response to ultra-fast laser pulses as observed in pump–probe spectroscopy, and for observing the coupling of electronic excitations to the vibrations of the nuclei in real time [6–16].

A key point for the accuracy of TDDFT and, thus a most meaningful comparison with experiments, is the choice of the time-dependent exchange-correlation (TD-XC) functional. Therefore, the improvement of existing approximations has been in the focus of recent active research [5, 17–21]. To fully assess the quality of XC functionals and systematically improve over existing ones, it is critical to control the numerical precision of the calculations. Without this, it is generally not possible to evaluate whether errors arise from limitations of the underlying method (here the XC treatment), from approximations made in the implementation, or from the actual computation. The quality of results relies on the choice of the basis employed to represent KS wavefunctions, on the description of core electrons (all-electron or frozen core), and of the potential shape (full potential or pseudo potential). In this sense, with its all-electron, full-potential LAPW + lo approach, `exciting` has proven to be one of the most accurate *ab initio* codes [22], capable of reaching micro-Hartree precision [23]. Furthermore, it is a user-friendly code with a growing community, and offers plenty of tuto-

rials on its implementations [24]. Nevertheless, up to now, TDDFT is available in `exciting` only in its LR formulation [25] while RT-TDDFT is still missing.

In this paper, we fill this gap and present our implementation of RT-TDDFT in the `exciting` code. This work also serves the purpose of making results reproducible by providing details of our implementation. These are given in section 2 after a summary of the theory behind. In section 3, we provide benchmarks by comparing our results with those obtained by the Octopus code [26], while more examples can be found in the appendix. In section 4, we demonstrate three interesting features of our implementation, namely (1) an analysis of the behavior of MoS<sub>2</sub> after excitation with a laser pulse, (2) a study of the third harmonic generation in silicon, and (3) a simulation of a pump–probe experiment in diamond. Finally, in section 5, we draw our conclusions.

## 2. Theory and implementation

We start by considering a physical system with periodic boundary conditions subjected to an electric field  $\mathbf{E}(t)$  with spatial variations on a scale much larger than the periodicity, and hence treated constant in space. The standard inclusion of  $\mathbf{E}(t)$  in the KS Hamiltonian would be by addition of a dipole term  $\mathbf{r} \cdot \mathbf{E}(t)$  that would break the desired periodicity. In this case, it is advantageous to employ the velocity-gauge [9, 27–29]:

$$\hat{H}(\mathbf{r}, t) = \frac{1}{2} \left( -i\nabla + \frac{1}{c} \mathbf{A}(t) \right)^2 + v_{\text{KS}}(\mathbf{r}, t), \quad (1)$$

where  $\mathbf{A}(t)$  is the vector potential, given in this gauge by  $\mathbf{A}(t) = -c \int_0^t \mathbf{E}(t') dt'$ ,  $c$  is the speed of light, and  $v_{\text{KS}}$  is the TD-KS potential, a sum of the TD ionic, Hartree and XC potentials. We assume here the adiabatic approximation for the TD-XC potential [30, 31]. A KS wavefunction  $\psi_{j\mathbf{k}}(\mathbf{r}, t)$  labeled with index  $j$  and associated to a wavevector  $\mathbf{k}$  evolves as

$$\hat{H}(\mathbf{r}, t) \psi_{j\mathbf{k}}(\mathbf{r}, t) = i \frac{\partial}{\partial t} \psi_{j\mathbf{k}}(\mathbf{r}, t). \quad (2)$$

In `exciting`, each KS wavefunction is expanded in terms of the LAPW + lo basis set with coefficients  $C_{j\mathbf{k}}(t)$ :

$$|\psi_{j\mathbf{k}}(t)\rangle = \sum_{\mathbf{G}} C_{j\mathbf{k}\mathbf{G}}(t) |\phi_{\mathbf{G}+\mathbf{k}}\rangle + \sum_{\gamma} C_{j\mathbf{k}\gamma}(t) |\phi_{\gamma}\rangle, \quad (3)$$

where  $|\phi_{\mathbf{G}+\mathbf{k}}\rangle$  and  $|\phi_{\gamma}\rangle$  represent the LAPW part of the basis and the local orbitals (lo), respectively;  $\mathbf{G}$  is a reciprocal lattice vector. Since the basis consists of two parts, i.e., LAPWs and lo's, the Hamiltonian ( $H_{\mathbf{k}}$ ) and overlap ( $S_{\mathbf{k}}$ ) matrices have a block structure, exemplified for the Hamiltonian, as

$$\begin{bmatrix} \langle \phi_{\mathbf{k}+\mathbf{G}} | \hat{H}(t) | \phi_{\mathbf{k}+\mathbf{G}'} \rangle & \langle \phi_{\mathbf{k}+\mathbf{G}} | \hat{H}(t) | \phi_{\gamma'} \rangle \\ \langle \phi_{\gamma} | \hat{H}(t) | \phi_{\mathbf{k}+\mathbf{G}'} \rangle & \langle \phi_{\gamma} | \hat{H}(t) | \phi_{\gamma'} \rangle \end{bmatrix}, \quad (4)$$

where each block is a dense matrix. Denoting with  $\mu$  and  $\nu$  generic indexes that can be associated with an LAPW or lo, following equation (1), an arbitrary element  $[H_{\mathbf{k}}(t)]_{\mu\nu} = \langle \phi_{\mu} | H(t) | \phi_{\nu} \rangle$  can be written as:

$$[H_{\mathbf{k}}(t)]_{\mu\nu} = \frac{1}{2} \langle \nabla \phi_{\mu} | \nabla \phi_{\nu} \rangle + \langle \phi_{\mu} | v_{\text{KS}}(t) | \phi_{\nu} \rangle + \frac{\mathbf{A}^2(t)}{2c^2} [S_{\mathbf{k}}]_{\mu\nu} - \frac{i}{c} \mathbf{A}(t) \cdot \langle \phi_{\mu} | \nabla | \phi_{\nu} \rangle. \quad (5)$$

The procedure to obtain  $\langle \nabla \phi_{\mu} | \nabla \phi_{\nu} \rangle$ ,  $\langle \phi_{\mu} | v_{\text{KS}}(t) | \phi_{\nu} \rangle$ , and  $[S_{\mathbf{k}}]_{\mu\nu}$  is detailed in reference [25]; the momentum matrix elements,  $\langle \phi_{\mu} | -i\nabla | \phi_{\nu} \rangle$ , are calculated as described in references [32, 33]. A summary is provided in appendix F.

With the definition of the basis, the integration of equation (2) reduces to the problem of finding how  $C_{j\mathbf{k}}(t)$  propagate in time. For this, many approaches are available [34–36]. Apart from the classical Runge–Kutta method for differential equations, we have implemented the following propagators: (i) simple exponential, (ii) exponential at the midpoint, (iii) approximate enforced time-reversal symmetry, (iv) commutator-free Magnus expansion of 4th order, and (v) exponential using a basis of the Hamiltonian's eigenvectors. To illustrate how our implementation works, we choose the simple exponential propagator, while appendix B details the other cases.

The evolution of KS wavefunctions in terms of a propagator  $\hat{U}(t + \Delta t, t)$  is:

$$|\psi_{j\mathbf{k}}(t + \Delta t)\rangle = \hat{U}(t + \Delta t, t) |\psi_{j\mathbf{k}}(t)\rangle, \quad (6)$$

where

$$\hat{U}(t + \Delta t, t) = \hat{T} \left[ \exp \left( -i \int_t^{t+\Delta t} d\tau \hat{H}(\tau) \right) \right], \quad (7)$$

$\hat{T}$  being the time-ordering operator. For the simple exponential propagator,  $\hat{U}(t + \Delta t, t)$  is regarded purely as  $\exp[-i\Delta t\hat{H}(t)]$ , the approximation being better, the smaller the time step  $\Delta t$  is. For this propagator, the following expression dictates the evolution of  $C_{j\mathbf{k}}(t)$ :

$$C_{j\mathbf{k}}(t + \Delta t) = \exp[-i\Delta t S_{\mathbf{k}}^{-1} H_{\mathbf{k}}(t)] C_{j\mathbf{k}}(t). \quad (8)$$

The matrix exponential in equation (8) is approximated by a Taylor expansion up to the order defined by the user (4 is the default).

### 2.1. Dielectric and optical-conductivity tensors

The dielectric and optical properties are quantities that can be measured by various experimental probes. They are also of main interest in LR-TDDFT calculations. To obtain them with RT-TDDFT, the behavior of the macroscopic current density,  $\mathbf{J}(t)$ , in response to an external field needs to be evaluated. For the case of local and semilocal KS functionals,  $\mathbf{J}(t)$  can be obtained as

$$\mathbf{J}(t) = \frac{i}{\Omega} \sum_{j\mathbf{k}} w_{\mathbf{k}} f_{j\mathbf{k}} \langle \psi_{j\mathbf{k}}(t) | \nabla | \psi_{j\mathbf{k}}(t) \rangle - \frac{N\mathbf{A}(t)}{c\Omega}, \quad (9)$$

where  $N$  is the number of valence electrons in the unit cell with volume  $\Omega$ ,  $w_{\mathbf{k}}$  is the weight of the considered  $\mathbf{k}$ -point, and  $f_{j\mathbf{k}}$  is the occupation number of the corresponding KS state. After Fourier transform, we obtain the components of the optical conductivity

$$J_{\alpha}(\omega) = \sum_{\beta} \sigma_{\alpha\beta}(\omega) E_{\beta}(\omega) \quad (10)$$

and the dielectric tensor  $\varepsilon$

$$\varepsilon_{\alpha\beta}(\omega) = \delta_{\alpha\beta} + \frac{4\pi i \sigma_{\alpha\beta}(\omega)}{\omega}, \quad (11)$$

where the indexes  $\alpha, \beta$  indicate the Cartesian directions  $x, y$ , or  $z$ . It is convenient to consider an impulsive electric field  $E_0\delta(t)$  in a specific direction  $\alpha$  such that  $E_{\alpha}(\omega) = E_0$ , and  $\sigma_{\beta\alpha}(\omega)$  is the ratio  $J_{\beta}(\omega)/E_{\alpha}(\omega)$ . This is known as the transverse geometry [9]. To understand its physical meaning, we look at the interface between the studied material and the vacuum, where the electric field comes from. Transverse geometry means that the field direction is parallel to the interface. Conversely, in the longitudinal geometry the electric field is perpendicular to the interface [9]. In this case, the displacement fields  $\mathbf{D}(t)$  inside and outside the system are related to each other through the surface charge, as given by the boundary conditions for electromagnetic fields [37]. Following references [9, 27], and [28], we consider the external component of the vector potential in the longitudinal geometry as given by  $\mathbf{A}_{\text{ext}}(t) = -cD_0\theta(t)\mathbf{e}_{\alpha}$  or, equivalently, by  $\mathbf{D}(t) = -(1/c)d\mathbf{A}_{\text{ext}}/dt = D_0\delta(t)\mathbf{e}_{\alpha}$ . The induced vector potential,  $\mathbf{A}_{\text{ind}}(t)$ , is obtained from the current density as

$$\frac{d^2\mathbf{A}_{\text{ind}}}{dt^2} = 4\pi c\mathbf{J}(t), \quad (12)$$

and the total vector potential  $\mathbf{A}(t)$ , appearing in the Hamiltonian, is calculated as the sum  $\mathbf{A}_{\text{ext}}(t) + \mathbf{A}_{\text{ind}}(t)$ .

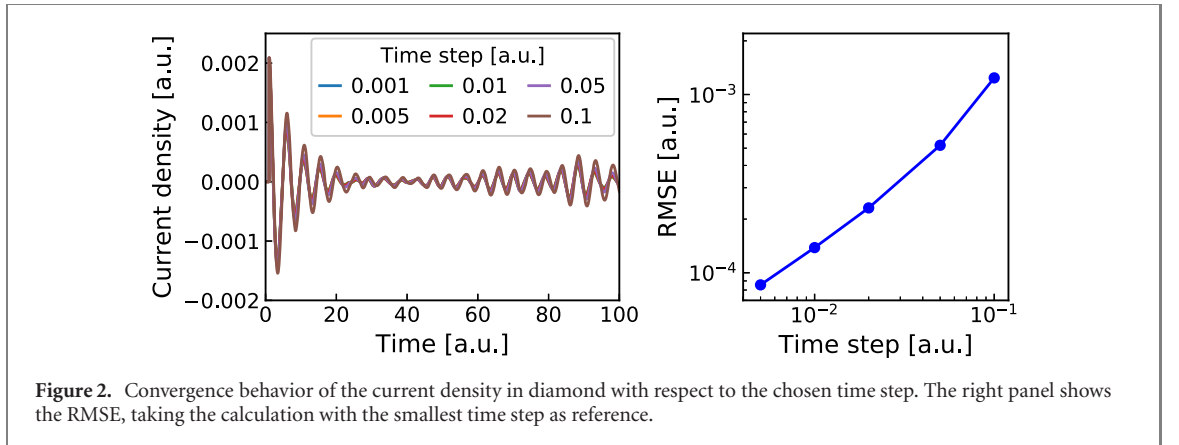
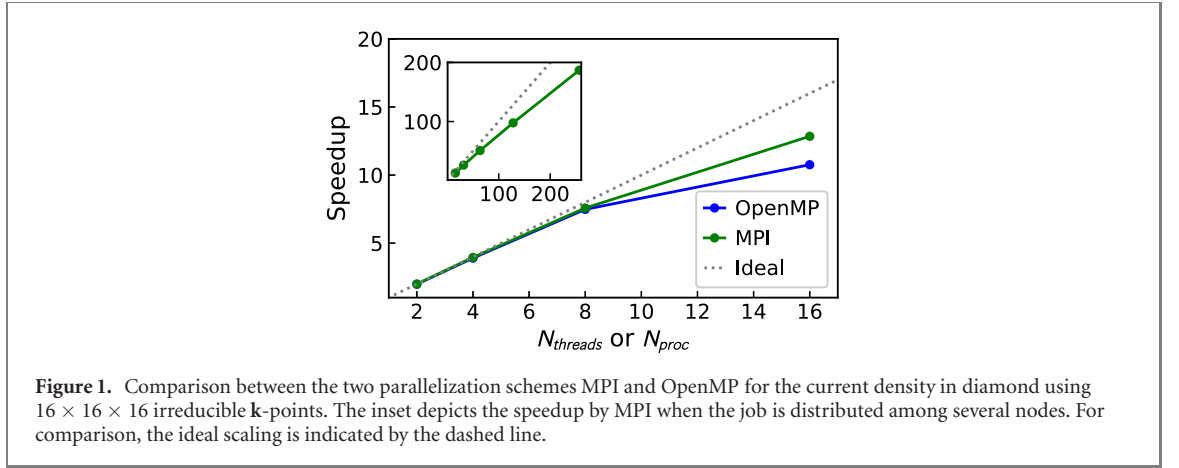
### 2.2. Number of excited electrons

A quantity of interest is the number of excited electrons after the interaction with a laser pulse [9, 11, 38–43]. In RT-TDDFT, the occupation number  $f_{j\mathbf{k}}$  of a KS state is kept fixed to its initial value. As the wavefunctions evolve, they are no longer eigenstates of  $\hat{H}(t)$ . It is possible to describe the number of excitations by projecting  $|\psi_{j\mathbf{k}}(t)\rangle$  onto the adiabatic ground state of  $\hat{H}(t)$ 's eigenfunctions [11, 39, 43] or onto the reference ground state at  $t = 0$  [9, 42, 43]. We opt here for the latter. Therefore, for a given  $\mathbf{k}$ -point, we define the number of electrons that have been excited to an unoccupied KS state, labeled  $j$ , as

$$m_{j\mathbf{k}}^e(t) = \sum_i f_{i\mathbf{k}} |\langle \psi_{j\mathbf{k}}(0) | \psi_{i\mathbf{k}}(t) \rangle|^2. \quad (13)$$

Similarly, the number of holes created in an occupied KS state  $j'$  can be specified as

$$m_{j'\mathbf{k}}^h(t) = f_{j'\mathbf{k}} - \sum_i f_{i\mathbf{k}} |\langle \psi_{j'\mathbf{k}}(0) | \psi_{i\mathbf{k}}(t) \rangle|^2. \quad (14)$$



Thus, the total number of excited electrons in a unit cell can be obtained by considering all the unoccupied states

$$N_{\text{exc}}(t) = \sum_{j\mathbf{k}}^{j \text{ unocc}} w_{\mathbf{k}} m_{j\mathbf{k}}^e(t) = \sum_{j\mathbf{k}}^{j \text{ occ}} w_{\mathbf{k}} m_{j\mathbf{k}}^h(t). \quad (15)$$

### 2.3. Parallelization

We follow the same parallelization strategy as already adopted in other parts of `exciting`, i.e., over  $\mathbf{k}$ -points [25]. In figure 1, we contrast the performance of two different levels of parallelization for calculations carried out on a single node with multiple processors: Open Multi-Processing (OpenMP) and Message Passing Interface (MPI). Although the speedup in both cases appears to be very close to the ideal one, MPI alone tends to be more efficient—also when compared to a hybrid parallelization (using both OpenMP and MPI, not shown in the figure). In the inset of figure 1, we depict the speedup of MPI when the calculations are distributed over a higher number of nodes, still showing fairly close to ideal scaling (speedup of 187 for 256 processors).

### 2.4. Convergence behavior

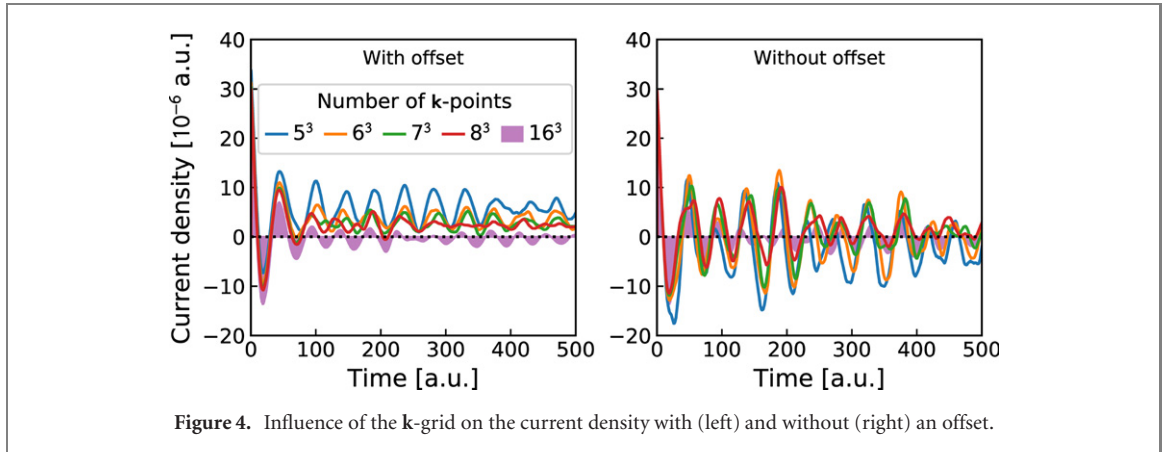
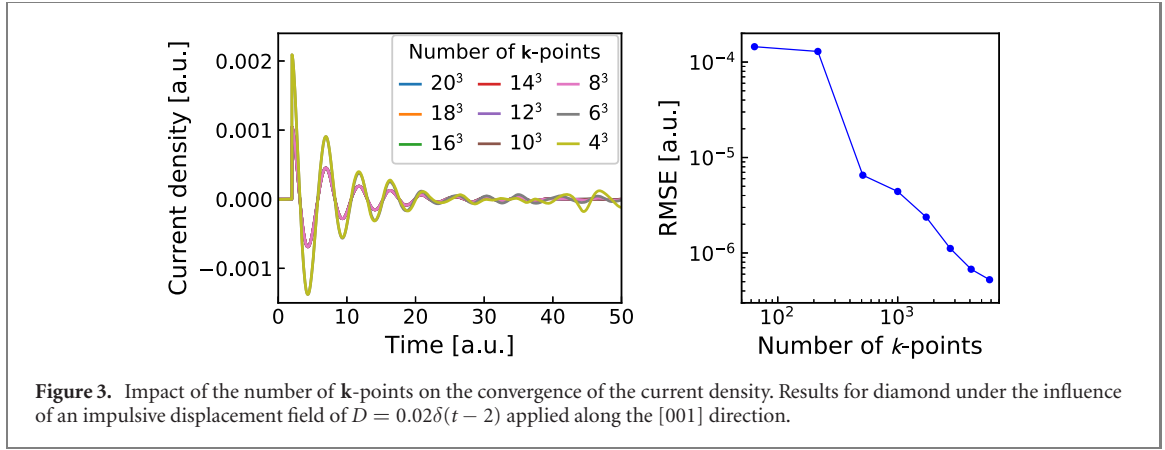
In the following, we analyze the impact of the three most important parameters governing the precision of RT-TDDFT calculations, namely: the time step, the number of  $\mathbf{k}$ -points, and the size of the basis. For a given value  $p$  of any of these parameters, we adopt the root-mean square error (RMSE)

$$\mathbb{E}_p = \sqrt{\frac{\int_0^T (j_p(t) - j_{\text{ref}}(t))^2 dt}{T}}, \quad (16)$$

to address the convergence behavior. Here,  $j_{\text{ref}}$  is a reference value for the current density, corresponding to the optimal parameter, and  $T$  stands for the end-time, up to which the evolution of KS wavefunctions is considered. In all calculations, a smearing of 0.001 Ha has been adopted.

#### 2.4.1. Time step

We consider diamond under an impulsive displacement field along the [001], direction given by  $D = 0.02\delta(t-1)$  in atomic units (a.u.). In figure 2, we show the current-density response to this field in the same direction. On the one hand, the curves are not easily distinguishable and apparently the current density is



insensitive to the time step, suggesting swift convergence of the results with decreasing time-step. Interestingly, time steps above 0.2 a.u. lead to divergence. On the other hand, taking the current density obtained with a time step of 0.001 a.u. as  $j_{\text{ref}}$  in equation (16), the RMSE depicted on the right side of the figure shows that the curves are not identical and the calculations become indeed more precise when the time step is reduced. The RMSE scales with the time step by a power law of 0.8. Although the value of the exponent depends on the material and on the method employed to propagate the wavefunctions, such power laws are found as a quite general trend, as already pointed out in reference [34]. A similar conclusion can be drawn in the case of silicon exposed to an electric field of two different forms (see figures D1 and D2 in appendix D.1).

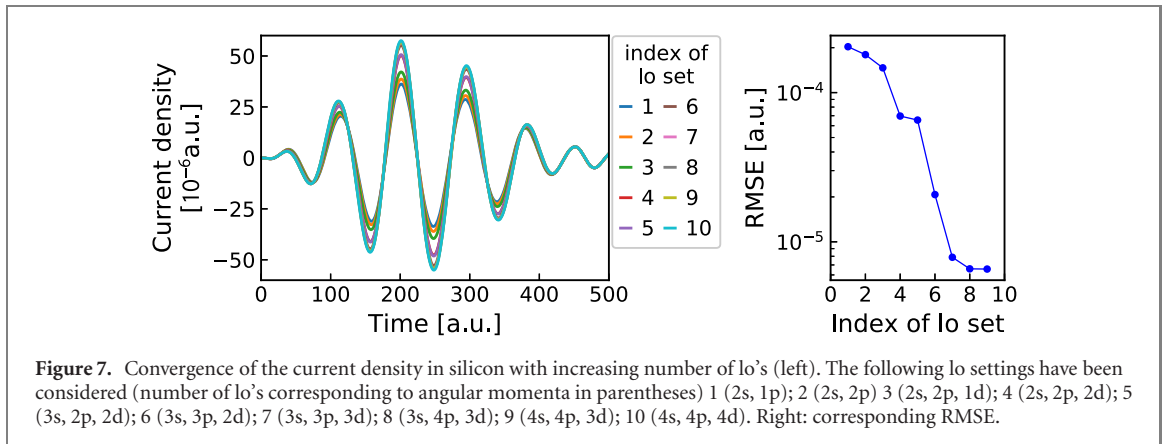
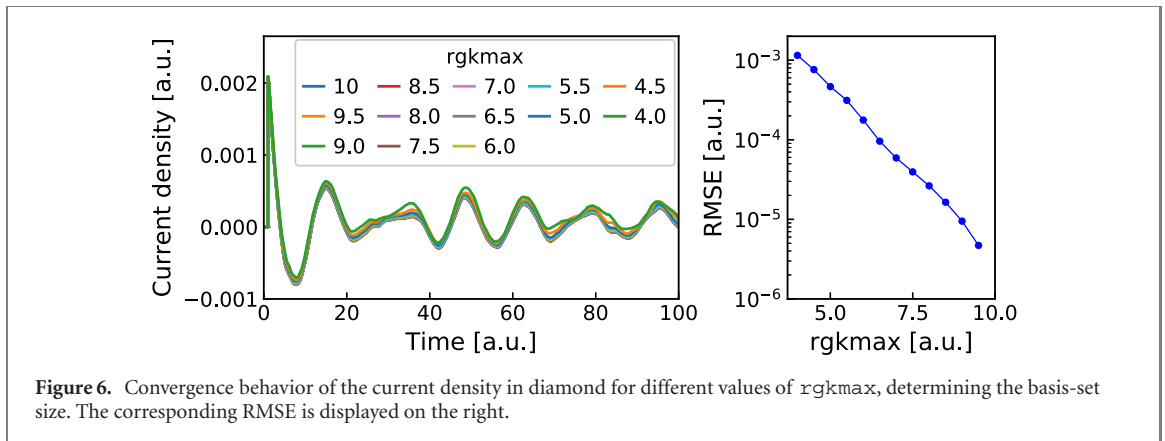
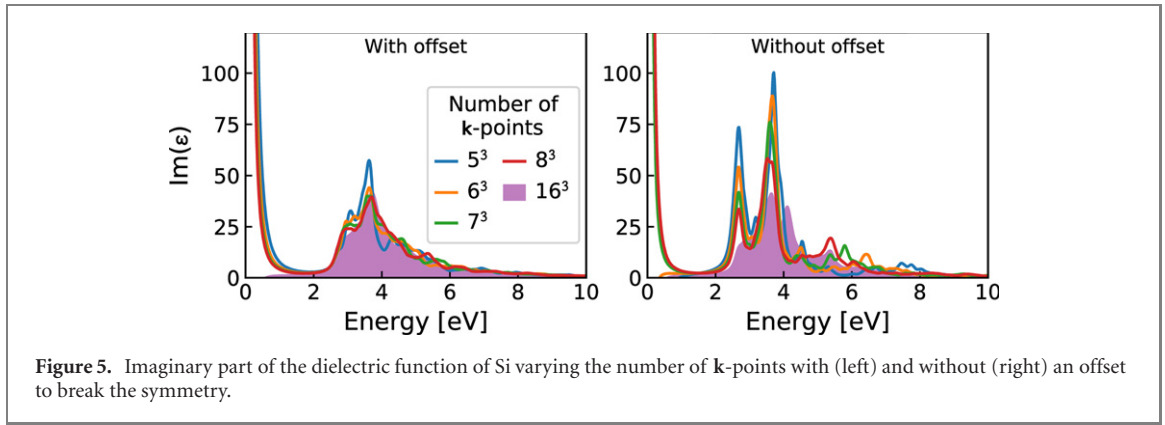
#### 2.4.2. Number of $\mathbf{k}$ -points

Analogous to ground-state calculations, the  $\mathbf{k}$ -grid has a direct impact on the quality of the current density (equation (9)) and the time-dependent electronic density, calculated as

$$n(\mathbf{r}, t) = \sum_{\mathbf{jk}} w_{\mathbf{k}} f_{\mathbf{jk}} |\psi_{\mathbf{jk}}(\mathbf{r}, t)|^2. \quad (17)$$

To illustrate its role, we consider diamond exposed to an impulsive displacement field  $D = 0.02\delta(t - 2)$  a.u. along the [001] direction. Figure 3 depicts how the number of  $\mathbf{k}$ -points affects the current density. Once more, the RMSE follows a power-law dependence on the investigated parameter (now, the number of  $\mathbf{k}$ -points), as seen in the right panel. The same applies to figures D3 and D4, where we consider Si excited by an impulsive field and a periodic function with a Gaussian-like envelope, respectively.

Another relevant aspect concerning the  $\mathbf{k}$ -grid is a possible offset that usually lowers the symmetry, leading to a set of symmetrically inequivalent  $\mathbf{k}$ -points. When the goal is, e.g., to obtain the dielectric function, the offset helps to avoid symmetrically redundant contributions. To exemplify the effect of such offset, we take as a test case silicon exposed to an electric field along the [001] direction given by  $E(t) = 0.001\delta(t - 0.16)$  a.u. Figure 4 depicts on the left side the current density for different  $\mathbf{k}$ -grids with an offset of  $0.01\mathbf{b}_1 + 0.45\mathbf{b}_2 + 0.37\mathbf{b}_3$  (where  $\mathbf{b}_i$  are the reciprocal lattice vectors). The graph on the right side shows the case when no offset is taken into account. Comparing both graphs, we verify that, apart from a vertical shift, the current density converges faster with respect to the  $\mathbf{k}$ -grid when an offset is considered. The vertical shift signals that the offset induces an artificial long-time behavior  $J(t \rightarrow \infty)$  that does not converge to zero for coarser grids. This is not



the case without an offset. Actually, in the linear regime, the summation in (9) should be ideally zero when the excitation field is removed. An offset may erroneously hamper cancellation of terms, this effect being much less pronounced when finer  $\mathbf{k}$ -grids are considered.

Figure 5 shows an equivalent comparison for the imaginary part of the dielectric function, calculated from the Fourier transform of the current density, as given in equation (11). We note a 'fake' plasmon at smaller frequencies (0–2 eV). This has already been reported in the literature in similar calculations employing the velocity-gauge [9, 27, 29, 44] and can be suppressed e.g., by using very dense  $\mathbf{k}$ -grids [9, 39]. When no offset is included, the convergence with respect to the number of  $\mathbf{k}$ -points is slower. In contrast, when an offset is taken into account, calculations with a  $\mathbf{k}$ -grid of  $8 \times 8 \times 8$  already show very similar results compared to doubling the points in each direction. Without the offset, transitions between valence and conduction band states tend to be sharper, and only a very high number of  $\mathbf{k}$ -points can describe those transitions that occur in the vicinity of  $\mathbf{k}$ -points with high-symmetry.

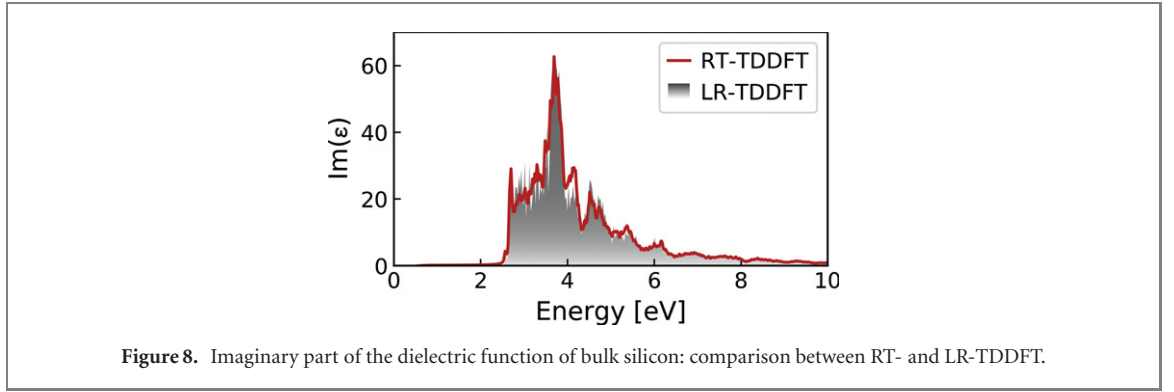


Figure 8. Imaginary part of the dielectric function of bulk silicon: comparison between RT- and LR-TDDFT.

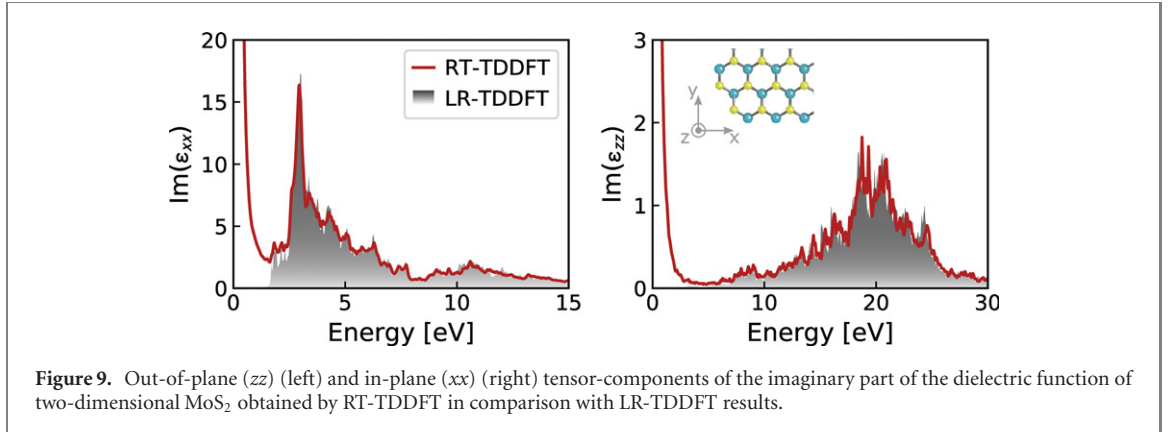


Figure 9. Out-of-plane ( $zz$ ) (left) and in-plane ( $xx$ ) (right) tensor-components of the imaginary part of the dielectric function of two-dimensional  $\text{MoS}_2$  obtained by RT-TDDFT in comparison with LR-TDDFT results.

### 2.4.3. Basis

In the case of LAPW + lo, the dimensionless parameter  $\text{r}gk\text{max}$  together with the number of lo's determine the quality of the basis. We need to inspect their impact on the convergence behavior separately. Starting with  $\text{r}gk\text{max}$ , we consider the current density in diamond exposed to an electric field  $E(t) = 0.02\delta(t - 1)$  a.u. along [001]. From figure 6, we conclude that the RMSE decreases exponentially when increasing  $\text{r}gk\text{max}$ . A similar behavior can also be observed in figure D6 (appendix D.3) for silicon exposed to a sinusoidal electric field modulated by a Gaussian-like envelope.

To check the role of lo's, we consider silicon subjected to the electric field

$$E(t) = E_m \sin^2 \left[ \pi \frac{(t - t_0)}{T_{\text{pulse}}} \right] \cos(\omega_0 t), \quad (18)$$

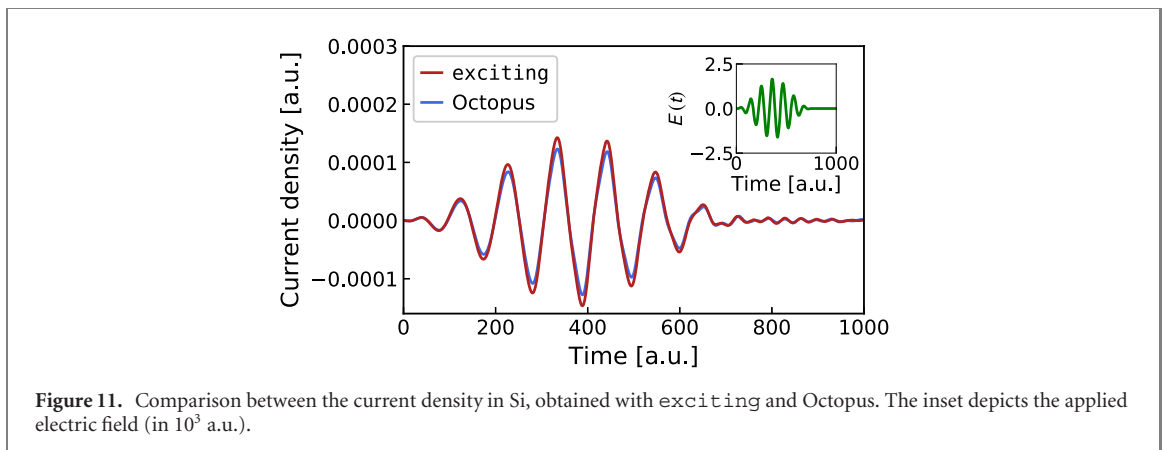
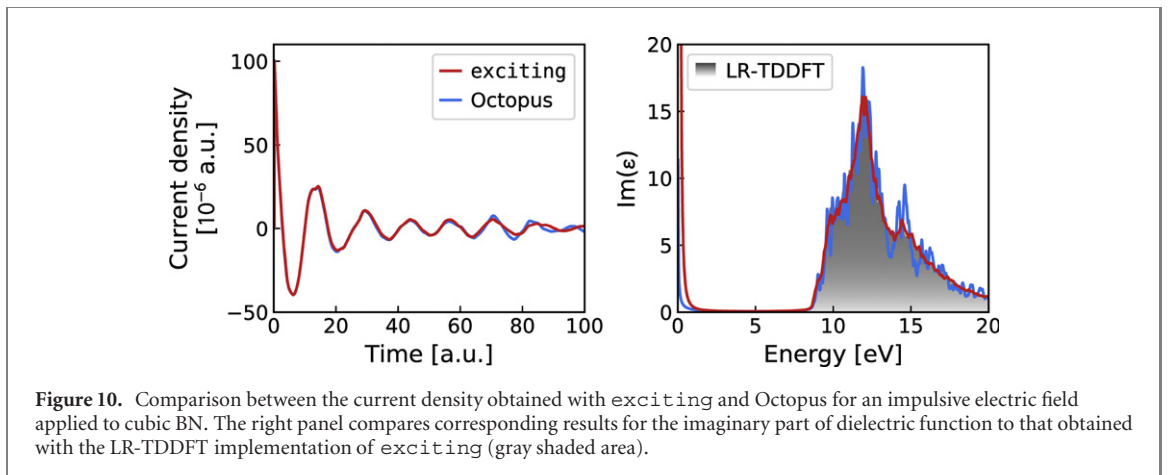
along [001] for  $t_0 \leq t \leq T_{\text{pulse}}$ , and 0 otherwise. This function describes a periodic wave with angular frequency  $\omega_0$  modulated by a Gaussian-like function, corresponding to a laser shape frequently employed in experiment. We choose,  $E_m = 1$ ,  $\omega_0 = 0.0628$ ,  $t_0 = 2$ , and  $T_{\text{pulse}} = 452$ , all quantities in a.u. In figure 7, we show how the current density changes when enhancing the basis with more lo's. Adding lo's with  $p$  or  $d$  character tends to improve the precision more than lo's with  $s$  character. lo's with other character were found to have very little impact, thus these results are not shown here.

## 3. Benchmark results

In this section, we present a benchmark of our implementation, contrasting the imaginary part of the dielectric function obtained with equation (11) with that of the LR-TDDFT, employing the adiabatic local-density approximation (ALDA) as already implemented in `exciting` [25]. We also compare the current density obtained with our implementation with results from Octopus [26].

### 3.1. Comparison of RT- and LR-TDDFT: dielectric function

As prototypical materials for our initial benchmark, we choose silicon and two-dimensional  $\text{MoS}_2$ . The imaginary part of their dielectric functions are given in figures 8 and 9, respectively. In the RT-TDDFT calculations, we considered an impulsive electric field with an amplitude small enough to not induce deviations from the linear regime. Apart from the already commented 'fake' plasmon in RT-TDDFT for smaller frequencies, we



observe overall a remarkable agreement between both results. A similar comparison for diamond is provided in figure E1.

### 3.2. Comparison with the Octopus code

Octopus has been one of the first codes to evaluate the propagation of KS wavefunctions within the framework of RT-TDDFT [3, 26, 27, 34]. Hence, it is a most suitable package to benchmark our results, even though it employs a different scheme to solve the KS equations, namely pseudo-potentials combined with a real-space mesh [26]. On the left side of figure 10, we depict the current density in cubic BN as response to an impulsive electric field. The agreement between the results of `exciting` and Octopus is impressive. On the right side, we provide the imaginary part of the dielectric function. This serves as well as a measure of how similar the Fourier-transforms of both curves are. We show also the result from our LR-TDDFT calculation, depicted as gray-shaded area. Once again, the agreement is excellent.

As a second benchmark, we depict in figure 11 the current density in Si exposed to an electric field, whose expression follows equation (18) and is shown in the inset, and compare the result to that obtained with Octopus. An interesting aspect here is that this field is strong enough to induce a nonlinear response, as it can be seen from the residual current density (after  $t = 700$  a.u., when the external field turns to zero). Also in this nonlinear regime, the agreement between `exciting` and Octopus is very good. Similar agreement is found for SiC, see figure E2.

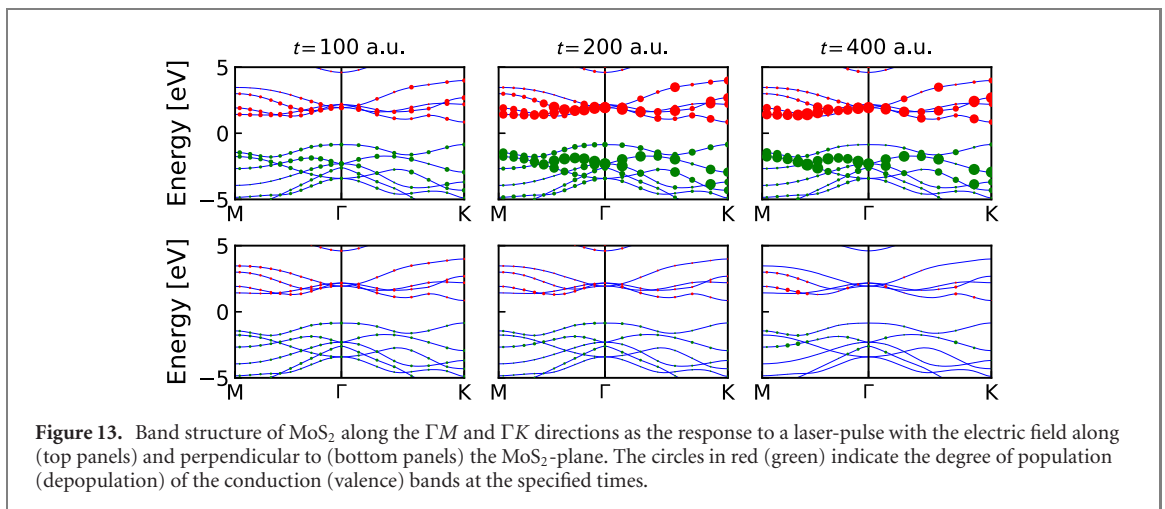
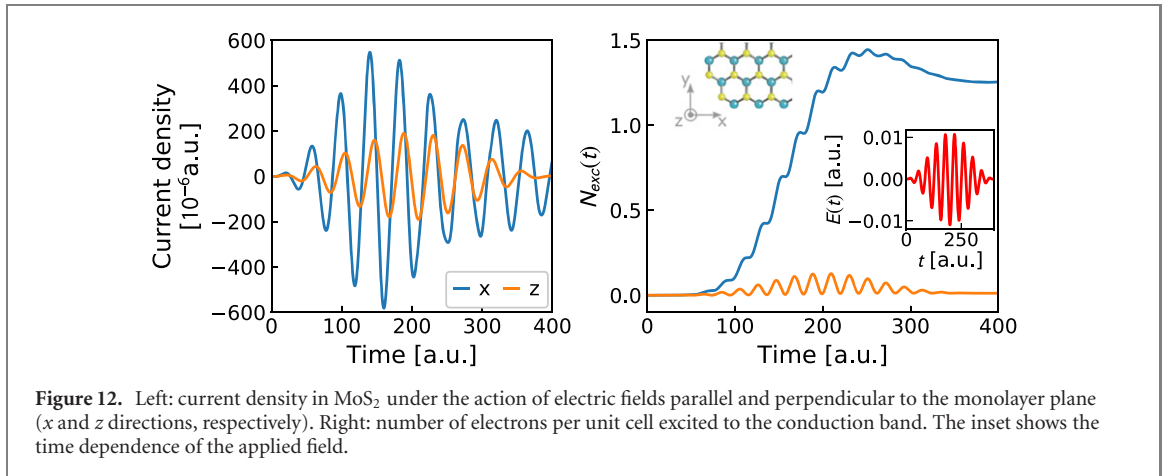
## 4. Implemented features

The RT-TDDFT implementation naturally provides the evolution of the KS system, i.e., KS energies and wavefunctions, charge density, and total energy as functions of time. In this section, we choose three features of our implementation which highlight it as an interesting tool to aid the interpretation of experiments.

### 4.1. Excitation dynamics

We start with the dynamics of an excitation in two-dimensional MoS<sub>2</sub> caused by a laser pulse with the electric field given by equation (18) and plotted in the inset on the right panel of figure 12. The pulse duration is set





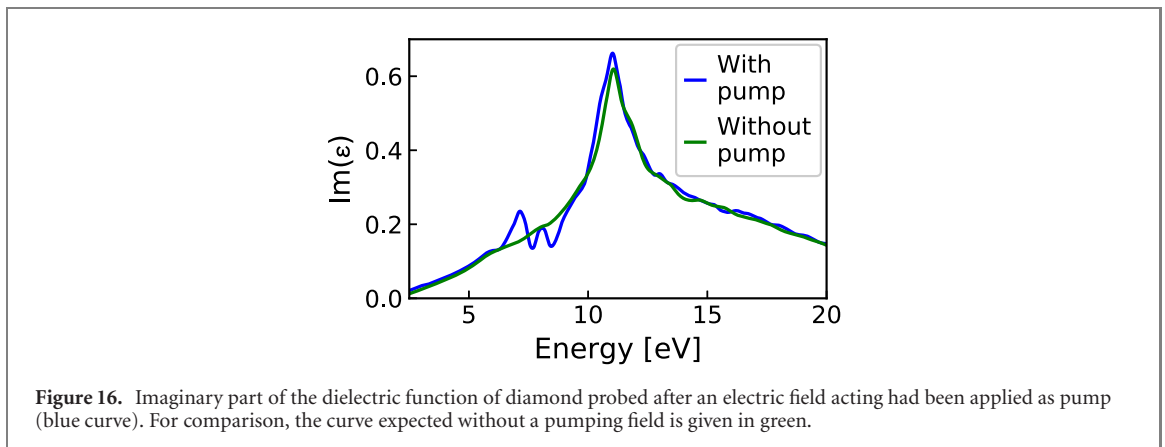
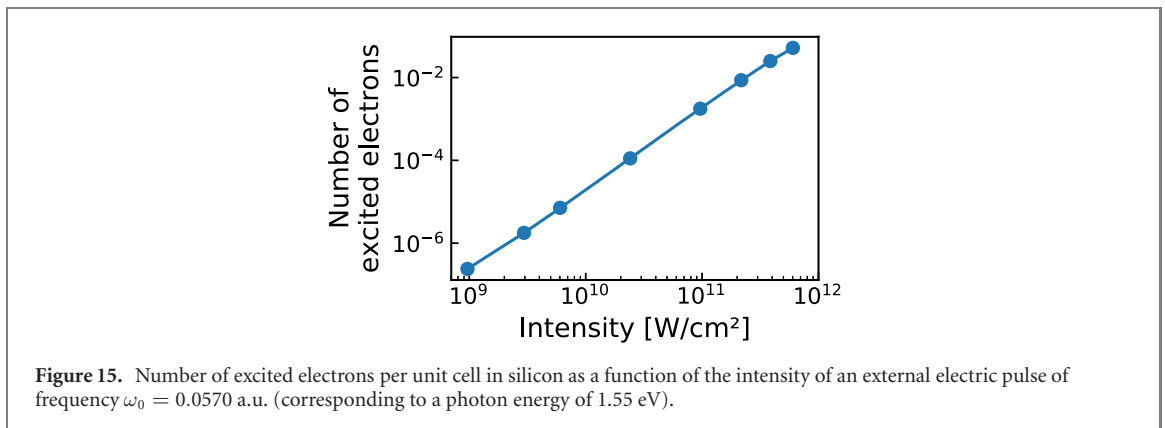
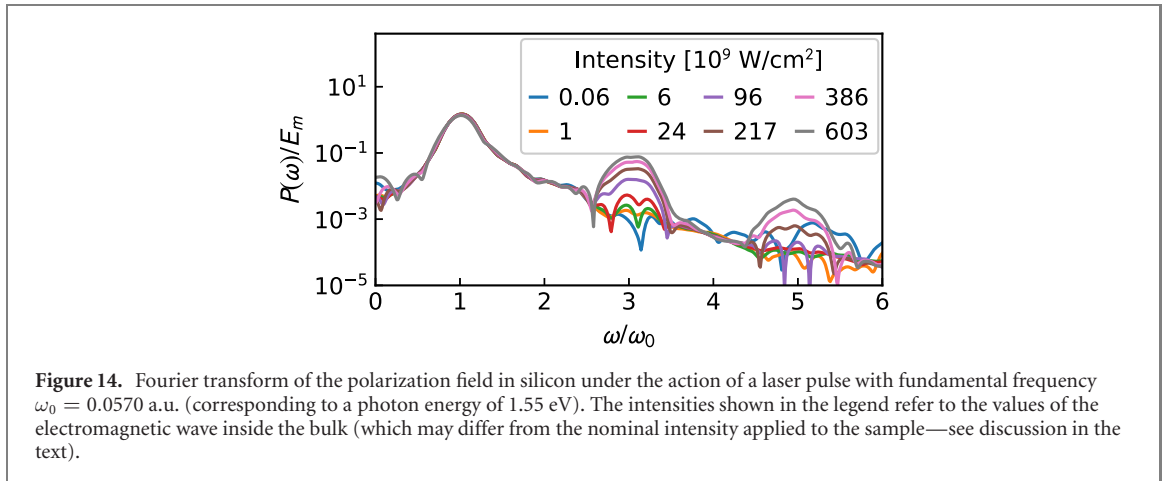
to  $T_{\text{pulse}} = 400$  a.u., the frequency to  $\omega_0 = 0.15$  a.u. (corresponding to a photon energy of 4.08 eV), and the peak intensity to  $E_m = 0.0107$  a.u. We carry out two calculations, one with the electric field parallel to the monolayer plane ( $x$  direction), the other one perpendicular to it ( $z$  direction). Figure 12 shows the current density in these two cases on the left, as well as the number of excited electrons on the right.

The current density is considerably higher in the case of in-plane polarization with a peak height being about 3 times larger. Some nonlinear effects are already observable. When we compare the number of excited electrons, we observe that, in the end, after the pulse is removed, 1.26 electrons per unit cell remain excited in the case of polarization along the  $x$  direction, but two orders of magnitude less, i.e., 0.012, for the  $z$  direction. We can understand this difference by the 2D nature of the material and can trace it back to the dielectric function (figure 9). The out-of-plane component  $\epsilon_{zz}$  at 4.08 eV is much higher than the in-plane component which means that, at this frequency, MoS<sub>2</sub> can absorb electromagnetic waves with the electric field parallel to the monolayer plane much better than perpendicular to it.

It is also interesting to observe from and to which bands the electrons are excited. In figure 13 we show for three different times, i.e.,  $t = 100, 200$  and  $400$  a.u. how the excitations are distributed over the  $k$ -space. In the top panels, we provide the results for the  $x$ -polarization and in the bottom panels for the  $z$ -polarization. In the case of in-plane polarization, some excitations are present at  $t = 100$  a.u.; many more electrons become excited at  $t = 200$  a.u., followed by a decrease thereafter. Interestingly, around the  $\Gamma$  and  $K$  points, the holes tend to be formed not on the valence-band top, but in deeper-lying bands, whereas at the  $M$  point, the holes are predominantly at the top one. In the case of the perpendicular polarization, there is almost no difference between the excitations at times  $t = 100$  a.u. and  $t = 200$  a.u. In the end, only a few excitations remain, and they are not concentrated at the band edges, but rather in deeper- and higher-lying bands, respectively.

#### 4.2. Non-linear response

We now analyze the response of silicon exposed to an electric field along the [001] direction whose expression follows equation (18), with the parameters  $\omega_0 = 0.0570$  a.u. (corresponding to a photon energy of 1.55 eV),



$T_{\text{pulse}} = 744$  a.u. = 18.0 fs, and  $t_0 = 0$ , according to reference [9]. The amplitude  $E_m$  is varied so that we can observe a progression from the linear to the nonlinear regime.

In figure 14, we depict the Fourier-transform of the polarization field  $P = (D - E)/(4\pi)$  normalized by the amplitude  $E_m$  of the applied electric field. The intensity of the electromagnetic wave  $I$  (in  $\text{W cm}^{-2}$ ) is obtained from the amplitude as  $I = 3.50941 \times 10^{16} E_m^2$ . It is important to recall that  $E_m$  stands for the amplitude of the electric field inside the bulk material. Due to reflection at the interface and boundary conditions, the electric field generated by the exciting laser may be different from  $E_m$ , sometimes even two orders of magnitude higher [9]. We can observe that, for intensities of  $9.6 \times 10^{10} \text{ W cm}^{-2}$  and higher, the third and even the fifth harmonic components are excited, and these components are obviously stronger the more intense the field is.

We also evaluate the number of excited electrons per unit cell,  $n_{\text{ex}}$ , at a sufficient large time after the electric field has been switched off, as shown in figure 15. We recognize that  $n_{\text{ex}}$  is connected to the intensity  $I$  of the electromagnetic wave by a power law, i.e.,

$$n_{\text{ex}} = CI^n. \quad (19)$$

By means of a least square fit, we find  $n = 1.94$ , which agrees with reference [43].

### 4.3. Dielectric function after laser pulse

We now simulate a pump–probe experiment, taking diamond as test material. The electric field of the pump pulse, given by equation (18), has a Gaussian-like envelope with width  $T_{\text{pulse}} = 644$  a.u., amplitude  $E_m = 2.2$  a.u., and fundamental frequency  $\omega_0 = 0.1$  a.u. (2.7 eV). At  $t = 700$  a.u., a weak impulsive electric field  $E(t) = 0.01\delta(t - 700)$  is applied as probe. We evaluate the dielectric function as indicated in equation (11), but taking the current density as the difference between the values after the pump and the probe ( $J_{\text{pump-probe}}$ ) and the pump pulse  $J_{\text{pump}}$ , as obtained from two separate calculations. In figure 16, we can identify that the main effect of the pump field is to change the absorption spectrum in the region between 6 and 11 eV, especially around the third harmonic component (7.1 eV).

## 5. Conclusions

In this paper, we have presented the implementation of RT-TDDFT in the full-potential LAPW + lo package `exciting`, providing the underlying theory and details on the convergence behavior as well as parallelization performance. As benchmarks, we have compared our results with those obtained with the Octopus code as well as LR-TDDFT results from `exciting`, finding excellent agreement in all cases. We have shown three examples of applications how our implementation could be used for the interpretation of experiments. These are the excitation dynamics of a material upon radiation with a laser pulse, the non-linear response of a material to laser pulses, and the dielectric function after a pump pulse. The implementation is included in the latest release, `exciting oxygen`, and the code can be downloaded for free from the `exciting` webpage [24]. All data presented here are available in the NOMAD Repository [45, 46] (DOI: [10.17172/NOMAD/2021.01.20-1](https://doi.org/10.17172/NOMAD/2021.01.20-1)).

## Acknowledgments

This work was supported by the Deutsche Forschungsgemeinschaft (DFG)-Projektnummer 182087777-SFB 951. We thank Keith Gilmore, Santiago Rigamonti, Sven Lubeck and, Felix Henneke for the critical review of this manuscript. Alexander Buccheri and Sebastian Tillack are acknowledged for reviewing our code.

## Data availability statement

The data that support the findings of this study are openly available at the following URL/DOI: <https://dx.doi.org/10.17172/NOMAD/2021.01.20-1>.

## Appendix A. Input

In figure A1, we display as an example, the input file of MoS<sub>2</sub>. For the RT-TDDFT calculations, the most important elements are captured by the element `rt_tddft` within the excited-state module `xs`. Here, the input file defines as propagator CFM4 (commutator free Magnus of 4th order), with an evolution time starting at 0 (default) up to 400 a.u. (`endtime`), with steps of 0.05 a.u. (`timestep`). The vector potential  $\mathbf{A}(t)$ , assuming the transverse geometry (`a field = 'total'`), is described by the element `laser`. In this case, we have a field applied along the  $z$  axis, with Gaussian-like envelope as in equation (18), where  $A_m = 100$  a.u.,  $\omega_0 = 0.15$  a.u.,  $T_{\text{pulse}} = 400$  a.u.,  $t_0 = 0$  a.u., and a null extra phase for the term  $\cos(\omega_0 t)$ . The element `symmetry_break` defines an axis, given in Cartesian coordinates (`Cartesian = 'true'`), to break the crystal symmetry. The full reference of input variables and their meaning is provided at the `exciting` webpage [24].

## Appendix B. Propagators

In this section, expressions for the propagator  $\hat{U}(t + \Delta t, t)$  are provided. The derivations and assessments of their advantages or disadvantages can be found in references [34, 35], and [36]. We start with the most basic extension to the simple exponential (SE) propagator, namely the exponential at the midpoint (EMR, exponential at midpoint rule):

$$\hat{U}(t + \Delta t, t) = \exp \left[ -i\Delta t \hat{H} \left( t + \frac{\Delta t}{2} \right) \right], \quad (\text{B.1})$$

```

1 <input>
2 <title>MoS2</title>
3 <structure speciespath="." cartesian="true">
4 <crystal>
5 <basevect>0.00000 6.00933 0.00000</basevect>
6 <basevect>5.20423 3.00466 0.00000</basevect>
7 <basevect>0.00000 0.00000 30.00000</basevect>
8 </crystal>
9 <species speciesfile="Mo.xml" rmt="2.4">
10 <atom coord="0.00000 0.00000 0.00000"/>
11 </species>
12 <species speciesfile="S.xml" rmt="2.1">
13 <atom coord="3.46949 0.00000 2.96176"/>
14 <atom coord="3.46949 0.00000 -2.96176"/>
15 </species>
16 </structure>
17 <groundstate xctype="LDA_PW" ngridk="21 21 1">
18 <rgkmax="6.0d0" nempty="5">
19 </groundstate>
20 <xs xstype="RT-TDDFT">
21 <rt_tddft propagator="CFM4">
22 <timestep="0.05d0" endtime="400d0">
23 <calculateTotalEnergy="true">
24 <calculateNexc="true">
25 <laser afield="total">
26 <sinsq ampl="100.0d0" omega="0.15d0">
27 <phase="0.d0" t0="0.d0" Tpulse="400d0">
28 <direction="z"/>
29 </laser>
30 <symmetrybreak cartesian="true">
31 <axis> 0.0 0.0 1.0 </axis>
32 </symmetrybreak>
33 </rt_tddft>
34 </xs>
35 </input>

```

Figure A1. Example of input file (input.xml).

where, the extrapolation for obtaining the Hamiltonian  $\hat{H}(t + f\Delta t)$  at future times is:

$$\hat{H}(t + f\Delta t) = (1 + f)\hat{H}(t) - f\hat{H}(t - \Delta t). \quad (\text{B.2})$$

Another extension to the simple exponential propagator which keeps time-reversal symmetry to be approximately fulfilled (AETRS, approximated enforced time reversal symmetry) is

$$\hat{U}(t + \Delta t, t) = \exp \left[ -i\frac{\Delta t}{2}\hat{H}(t + \Delta t) \right] \exp \left[ -i\frac{\Delta t}{2}\hat{H}(t) \right]. \quad (\text{B.3})$$

Further improvement is provided by the so called commutator-free Magnus expansion of 4th order (CFM4):

$$\hat{U}(t + \Delta t, t) = \exp \left[ -i\Delta t(\alpha_1\hat{H}(t_1) + \alpha_2\hat{H}(t_2)) \right] \times \exp \left[ -i\Delta t(\alpha_2\hat{H}(t_1) + \alpha_1\hat{H}(t_2)) \right], \quad (\text{B.4})$$

where  $t_{1,2} = t + \left( \frac{1}{2} \mp \frac{\sqrt{3}}{6} \right) \Delta t$ , and  $\alpha_{1,2} = \frac{3 \mp 2\sqrt{3}}{12}$ .

A different approach is evaluating the exponential operator exactly rather than Taylor-expanding it. This can be done by taking into account an adiabatic basis formed by the eigenvectors of  $\hat{H}(t)$  (EH, exponential using eigenvectors of  $H$  as basis). It means that for each  $t$ , we solve

$$\hat{H}(t)|\phi_{jk}(t)\rangle = \varepsilon_{jk}(t)|\phi_{jk}(t)\rangle \quad (\text{B.5})$$

and then expand

$$|\psi_{jk}(t)\rangle = \sum_i \alpha_{ijk}(t)|\phi_{ik}(t)\rangle, \quad (\text{B.6})$$

where  $\alpha_{ijk}(t) = \langle \phi_i^k(t) | \psi_j^k(t) \rangle$ . Since

$$\hat{U}(t + \Delta t, t)|\phi_{mk}(t)\rangle = e^{-i\varepsilon_{mk}(t)\Delta t}|\phi_{mk}(t)\rangle, \quad (\text{B.7})$$

**Table C1.** Performance of each propagator in terms of computational time and RMSE. The time takes into account the action of the propagator  $\hat{U}(t + \Delta t, t)|\psi_{jk}(t)\rangle$  on all KS states over all  $\mathbf{k}$ -points. The time is normalized to the smallest one among the propagators. For the RMSE, the reference is the current density obtained with AETRS for time step of 0.0001 a.u. In parentheses, the number of empty states for EH and EHM.

Integrator	Time	RMSE [a.u.]
SE	1.00	$8 \times 10^{-7}$
EMR	1.04	$8 \times 10^{-7}$
RK4	1.08	$8 \times 10^{-7}$
EHM(5)	1.44	$2 \times 10^{-5}$
EH(5)	1.46	$2 \times 10^{-5}$
AETRS	1.92	$8 \times 10^{-7}$
CFM4	1.97	$8 \times 10^{-7}$
EH(50)	3.11	$1 \times 10^{-6}$
EHM(50)	3.16	$1 \times 10^{-6}$
EHM(100)	8.28	$9 \times 10^{-7}$
EH(100)	10.68	$9 \times 10^{-7}$

when considering  $\hat{U}(t + \Delta t, t)$  in the form of the simple exponential propagator, the action of the propagator, using equation (B.6), is

$$\hat{U}(t + \Delta t, t)|\psi_{jk}(t)\rangle = \sum_i \alpha_{ijk}(t) e^{-i\varepsilon_{mk}(t)\Delta t} |\phi_{mk}(t)\rangle. \quad (\text{B.8})$$

We further utilize then the expansion of  $|\phi_{mk}(t)\rangle$  in terms of our LAPW + lo basis.

Although the exponential operator is exactly obtained, i.e., without the need of a Taylor expansion, this approach now relies on an expansion in terms of the adiabatic basis and on the assumption of a simple exponential for the propagator. A first refinement can be provided if we employ the exponential at the midpoint (EHM), and then consider the adiabatic basis of  $\hat{H}(t + \Delta t/2)$ .

Finally, it is also possible to employ the classical integrator of differential equations, the Runge–Kutta method, where we consider here the 4th order, i.e.,

$$|\psi_{jk}(t + \Delta t)\rangle = |\psi_{jk}(t)\rangle - \frac{i\Delta t}{6}(k_1 + 2k_2 + 2k_3 + k_4) \quad (\text{B.9})$$

where

$$k_1 = S_k^{-1} H_k(t) |\psi_{jk}(t)\rangle, \quad (\text{B.10})$$

$$k_2 = S_k^{-1} H_k\left(t + \frac{\Delta t}{2}\right) \left[ |\psi_{jk}(t)\rangle + k_1 \frac{\Delta t}{2} \right], \quad (\text{B.11})$$

$$k_3 = S_k^{-1} H_k\left(t + \frac{\Delta t}{2}\right) \left[ |\psi_{jk}(t)\rangle + k_2 \frac{\Delta t}{2} \right], \quad (\text{B.12})$$

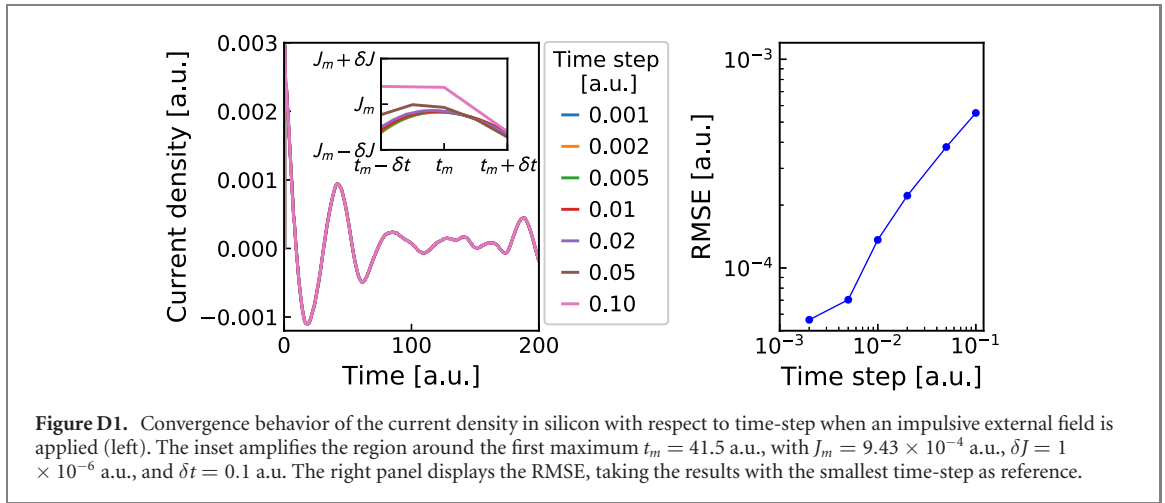
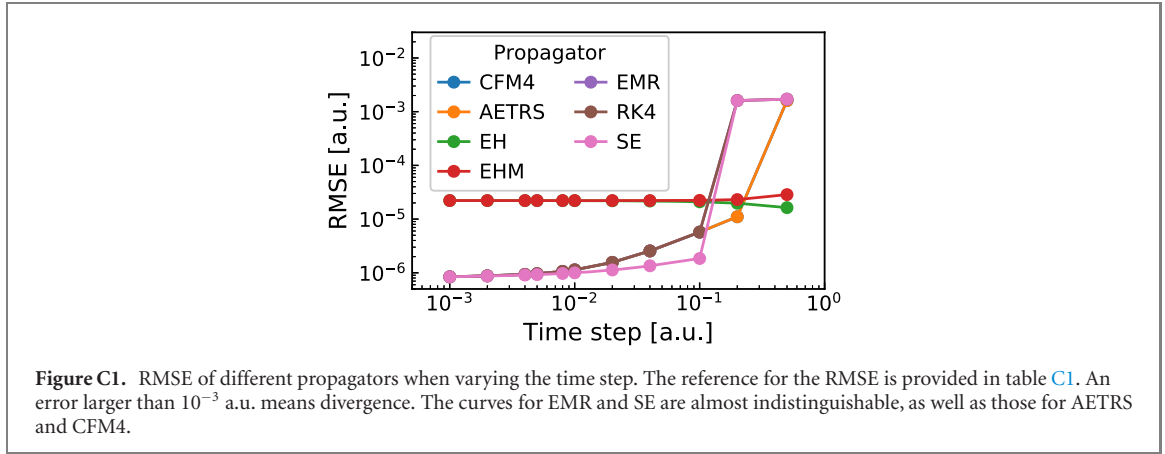
$$k_4 = S_k^{-1} H_k(t + \Delta t) \left[ |\psi_{jk}(t)\rangle + k_3 \Delta t \right]. \quad (\text{B.13})$$

## Appendix C. Performance

In table C1, we compare the computational time and the accuracy of the propagators.

For this analysis, we calculated diamond submitted to an impulsive electric field along the [001] direction  $E = 0.01\delta(t)$  in a.u. using a time step of 0.001 a.u. The time shown in table C1 has been averaged, for each propagator, over all the evolution steps, and then normalized with respect to the fastest method. To obtain the RMSE as given in equation (16), we chose as reference the current density of AETRS obtained for a much smaller time step of 0.0001 a.u. We can see that the best compromise between computational efficiency and accuracy is achieved by SE, EMR, and RK4. Also, the accuracy of EH and EHM is highly dependent on the number of excited states used to build the auxiliary basis of adiabatic eigenvectors.

In figure C1, we compare how the numerical accuracy of each propagator is affected by the time step, taking the same reference for the RMSE as before. For the sake of computational cost, EH and EHM were employed with five excited states. For small time steps, CFM4, AETRS, EMR, RK4 and SE show similar RMSE's. SE and EMR tend to diverge for smaller time steps, even though they present smaller RMSE's than other methods when not divergent. Surprisingly, the accuracy of EH and EHM is not very sensitive to the time step, and these propagators still converge for a step of 0.5 a.u., while all others diverge.



## Appendix D. More benchmarks on convergence behavior

### D.1. Convergence with respect to the time step

In figures D1 and D2, we show the convergence behavior of the current density in silicon, probing the size of the time step after an external electric field is applied along the [001] direction. In the first case, it is a delta function,  $E(t) = 0.1\delta(t - 0.5)$  a.u., while in the second case, it has a Gaussian-like envelop, equation (18), with the parameters  $E_m = 4.61 \times 10^{-4}$ ,  $\omega_0 = 0.0628$ ,  $t_0 = 2.0$ , and  $T_{\text{pulse}} = 452$  (in atomic units).

### D.2. Convergence behavior with respect to k-points

Figures D3 and D4 display the convergence behavior of the current density in silicon with respect to the  $\mathbf{k}$ -grid. The external electric fields are the same as in appendix D.1.

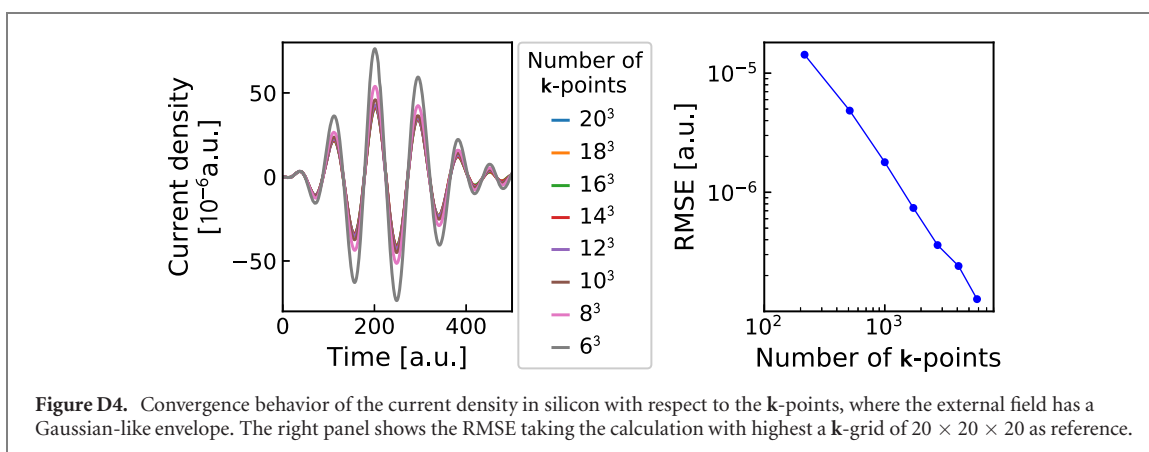
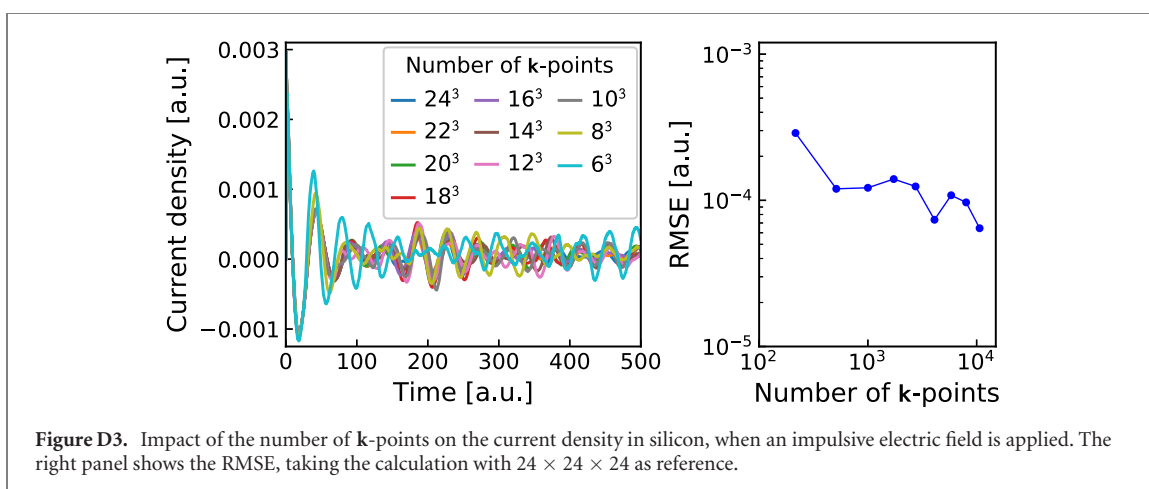
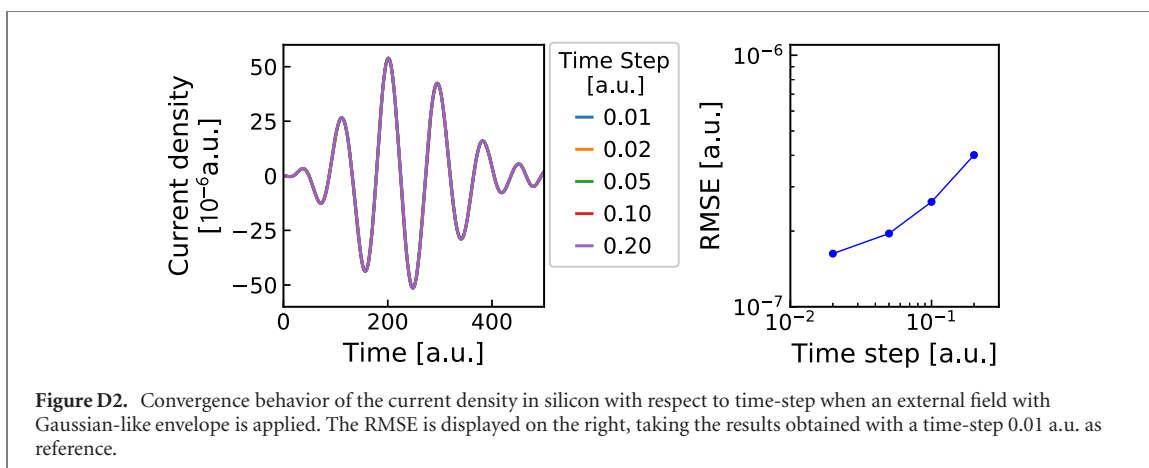
Figure D5 shows the influence of the number of  $\mathbf{k}$ -points on the dielectric function of carbon. These results have been obtained from a Fourier transform of those given in figure 3 (calculations up to a time of 5000 a.u.).

### D.3. Convergence with respect to basis-set size

Figure D6 displays the impact of the choice of the parameter `rgkmax` on the convergence behavior of the current density in silicon. The external electric field has a Gaussian-like envelope, as given by equation (18), with same parameters as in appendix D.1.

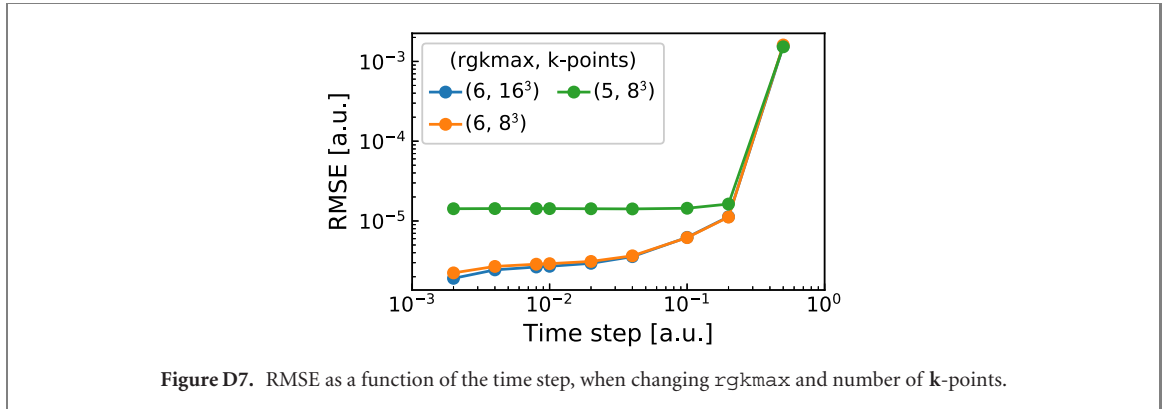
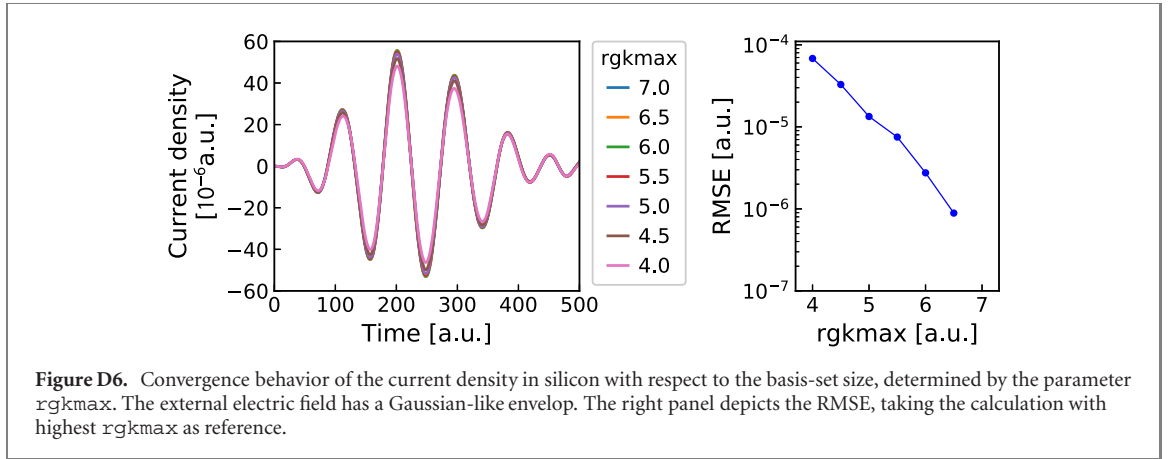
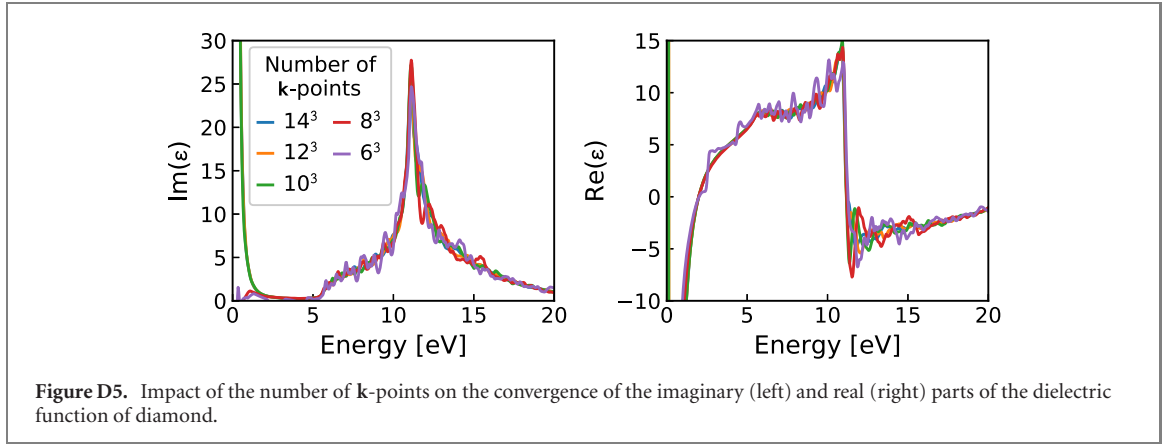
### D.4. Mutual dependence of convergence parameters

In figure D7, we compare the coupling between three convergence parameters, i.e., time step, number of  $\mathbf{k}$ -points, and `rgkmax`. The test considers the current density in diamond after an impulsive electric field along the [001] direction,  $E = 0.01\delta(t)$  (in a.u.). The panel shows the RMSE taking  $j_{\text{ref}}(t)$  obtained with a  $\mathbf{k}$ -mesh of  $16 \times 16 \times 16$ , `rgkmax` of 6.0 and a time step of 0.001 a.u. as reference.



### Appendix E. Benchmark results complementing section 3

Figure E1 displays how the imaginary part of the dielectric function of diamond obtained with RT-TDDFT compares with that from LR-TDDFT. In figure E2, we compare the current density in SiC obtained with `exciting` to the result by `Octopus`. The external field is a delta function applied along the  $[001]$  direction, i.e.,  $D(t) = 0.01\delta(t - 2)$  [a.u.]. The right side of the figure shows how the imaginary part of the dielectric function obtained from the RT-TDDFT calculations of the two codes compares with LR-TDDFT obtained with `exciting`.



## Appendix F. Matrix elements

Here, we briefly summarize how the matrix elements  $[H_{\mathbf{k}}(t)]_{\mu\nu}$ ,  $[S_{\mathbf{k}}(t)]_{\mu\nu}$  and  $\langle \phi_{\mu} | \nabla | \phi_{\nu} \rangle$  are computed. A complete description of the formalism can be found in references [25, 32, 33].

Following the notation of equation (4), we start with the local-orbital block (lo-lo) by considering a lo with index  $\gamma$  defined within muffin-tin  $\alpha_{\gamma}$  as a product of a radial function  $f_{\gamma}(r)$  and a spherical harmonic  $Y_{l_{\gamma}m_{\gamma}}$ . The Hamiltonian element can be expressed as

$$\langle \phi_{\gamma} | \hat{H}(t) | \phi_{\gamma'} \rangle = h_{\gamma\gamma'}(t) + \frac{\mathbf{A}^2(t)}{2c^2} [S_{\mathbf{k}}]_{\gamma\gamma'} - \frac{i}{c} \mathbf{A}(t) \cdot \langle \phi_{\gamma} | \nabla | \phi_{\gamma'} \rangle. \quad (\text{E.1})$$



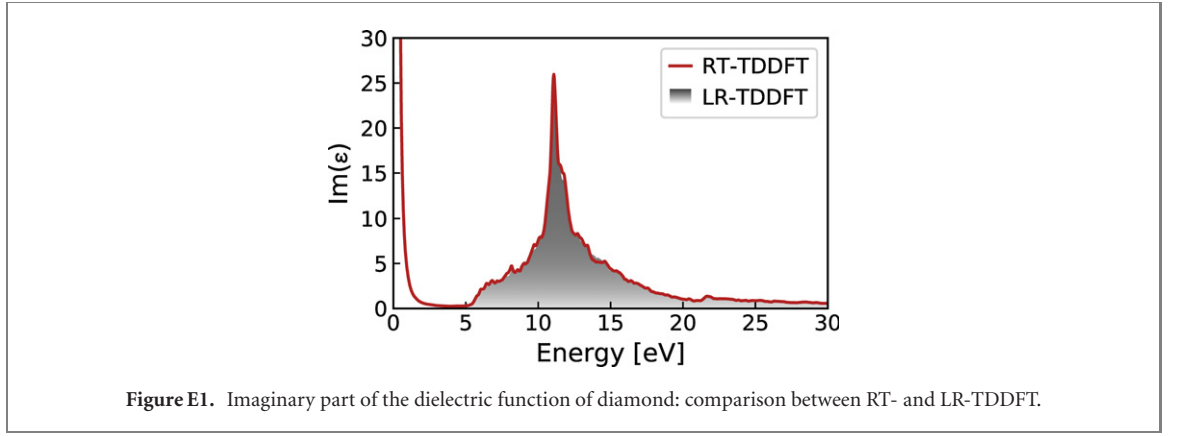


Figure E1. Imaginary part of the dielectric function of diamond: comparison between RT- and LR-TDDFT.

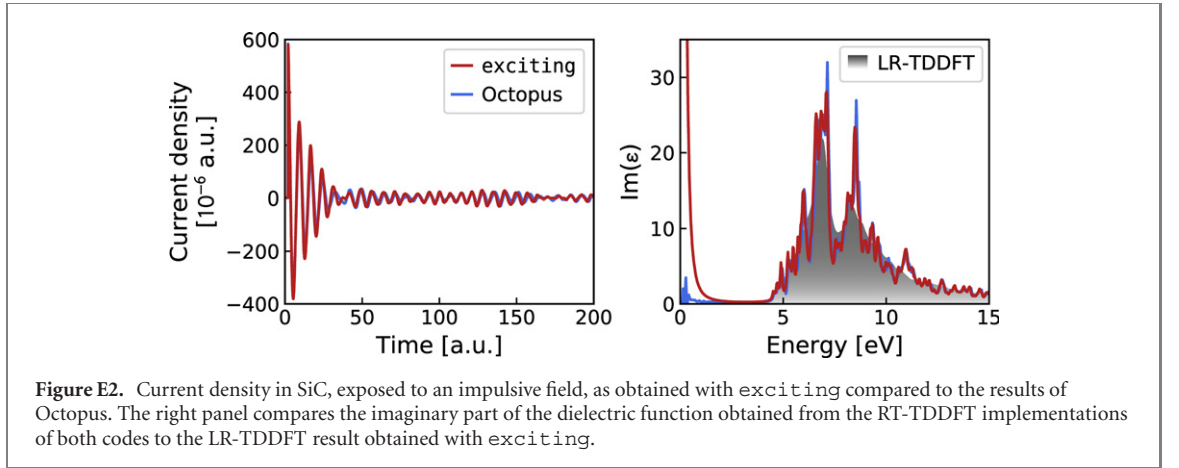


Figure E2. Current density in SiC, exposed to an impulsive field, as obtained with `exciting` compared to the results of `Octopus`. The right panel compares the imaginary part of the dielectric function obtained from the RT-TDDFT implementations of both codes to the LR-TDDFT result obtained with `exciting`.

The auxiliary matrix  $h$  is

$$\begin{aligned}
 h_{\gamma\gamma'}(t) = & \delta_{\alpha\gamma\alpha'}\delta_{l_\gamma l_{\gamma'}}\delta_{m_\gamma m_{\gamma'}} \int_0^{R_{\text{MT}}^\alpha} \left( \frac{df_\gamma^*}{dr} \frac{df_{\gamma'}}{dr} \right. \\
 & \left. + \frac{l_\gamma(l_\gamma + 1)}{r^2} f_\gamma^*(r)f_{\gamma'}(r)r^2 \right) r^2 dr \\
 & + \delta_{\alpha\gamma\alpha'} \sum_{lm} \mathcal{G}_{l_\gamma m_\gamma, l_{\gamma'} m_{\gamma'}}^{lm} \int_0^{R_{\text{MT}}^\alpha} (f_\gamma(r))^* v_{lm}(t) f_{\gamma'}(r) r^2 dr,
 \end{aligned} \quad (\text{E.2})$$

where  $\mathcal{G}_{l_\gamma m_\gamma, l_{\gamma'} m_{\gamma'}}^{lm}$  are the Gaunt coefficients,  $R_{\text{MT}}^\alpha$  is the radius of muffin-tin sphere  $\alpha$ , and  $v_{lm}(t)$  are the expansion coefficients of  $v_{\text{KS}}(t)$  in terms of real spherical harmonics. The elements of the overlap matrix are written as  $[\mathbf{S}_{\mathbf{k}}]_{\gamma\gamma'} = s_{\gamma\gamma'}$ , making use of an auxiliary matrix  $s$

$$s_{\gamma\gamma'} = \delta_{\alpha\gamma\alpha'}\delta_{l_\gamma l_{\gamma'}}\delta_{m_\gamma m_{\gamma'}} \int_0^{R_{\text{MT}}^\alpha} f_\gamma^*(r)f_{\gamma'}(r)r^2 dr. \quad (\text{E.3})$$

$\langle \phi_\gamma | \nabla | \phi_{\gamma'} \rangle$  are obtained by an expansion of  $\nabla \phi_{\gamma'}(\mathbf{r}) = \nabla f_{\gamma'}(r) Y_{l_\gamma m_{\gamma'}}(\hat{r})$  in terms of spherical harmonics

$$\nabla \phi_{\gamma'}(\mathbf{r}) = \sum_{lm} \left[ f_{\gamma'}^*_{l_\gamma m_\gamma, l_\gamma m_\gamma x}(r) \mathbf{e}_x + f_{\gamma'}^*_{l_\gamma m_\gamma, l_\gamma m_\gamma y}(r) \mathbf{e}_y + f_{\gamma'}^*_{l_\gamma m_\gamma, l_\gamma m_\gamma z}(r) \mathbf{e}_z \right] Y_{lm}(\hat{r}), \quad (\text{E.4})$$

and with this

$$\langle \phi_\gamma | \nabla | \phi_{\gamma'} \rangle = \delta_{\alpha\gamma\alpha'} \int_0^{R_{\text{MT}}^\alpha} r^2 dr (f_\gamma(r))^* \left[ f_{\gamma'}^*_{l_\gamma m_\gamma, l_\gamma m_\gamma x}(r) \mathbf{e}_x + f_{\gamma'}^*_{l_\gamma m_\gamma, l_\gamma m_\gamma y}(r) \mathbf{e}_y + f_{\gamma'}^*_{l_\gamma m_\gamma, l_\gamma m_\gamma z}(r) \mathbf{e}_z \right]. \quad (\text{E.5})$$

In the LAPW–LAPW block, the Hamiltonian elements,  $[H_{\mathbf{k}}(t)]_{\mathbf{G}\mathbf{G}'} = \langle \phi_{\mathbf{k}+\mathbf{G}} | \hat{H}(t) | \phi_{\mathbf{k}+\mathbf{G}'} \rangle$ , are

$$[H_{\mathbf{k}}(t)]_{\mathbf{G}\mathbf{G}'} = \frac{1}{2}(\mathbf{k} + \mathbf{G}) \cdot (\mathbf{k} + \mathbf{G}')\Theta(\mathbf{G} - \mathbf{G}') + v_{\text{KS}}(\mathbf{G} - \mathbf{G}', t) + \sum_{\alpha} \sum_{\nu\nu'} (\mathcal{A}_{\nu\mathbf{G}}^{\alpha\mathbf{k}})^* h_{\nu\nu'} \mathcal{A}_{\nu'\mathbf{G}'}^{\alpha\mathbf{k}} + \frac{\mathbf{A}^2(t)}{2c^2} [S_{\mathbf{k}}]_{\mathbf{G}\mathbf{G}'} - \frac{i}{c} \mathbf{A}(t) \cdot \langle \phi_{\mathbf{k}+\mathbf{G}} | \nabla | \phi_{\mathbf{k}+\mathbf{G}'} \rangle, \quad (\text{F.6})$$

where  $\Theta(\mathbf{G} - \mathbf{G}') = \langle \phi_{\mathbf{k}+\mathbf{G}} | \Theta(\mathbf{r}) | \phi_{\mathbf{k}+\mathbf{G}'} \rangle$  is a matrix element of the step function,  $\Theta(\mathbf{r})$ , defined as 0 in any muffin-tin and 1 in the interstitial region.  $\mathcal{A}_{\nu\mathbf{G}}^{\alpha\mathbf{k}}$  are the matching coefficients to ensure continuity of the basis functions at the muffin-tins sphere boundaries.  $v_{\text{KS}}$  is a matrix element of the KS potential times  $\Theta(\mathbf{r})$ :

$$v_{\text{KS}}(\mathbf{G} - \mathbf{G}', t) = \langle \phi_{\mathbf{k}+\mathbf{G}} | v_{\text{KS}}(\mathbf{r}, t) \Theta(\mathbf{r}) | \phi_{\mathbf{k}+\mathbf{G}'} \rangle. \quad (\text{F.7})$$

The overlap matrix elements in equation (F.6) can be expressed as

$$[S_{\mathbf{k}}]_{\mathbf{G}\mathbf{G}'} = \sum_{\alpha} \sum_{\nu\nu'} (\mathcal{A}_{\nu\mathbf{G}}^{\alpha\mathbf{k}})^* s_{\nu\nu'} \mathcal{A}_{\nu'\mathbf{G}'}^{\alpha\mathbf{k}}, \quad (\text{F.8})$$

where the auxiliary matrix  $s$  is defined analogously to equation (F.3). The same holds for  $h$  in equation (F.6) in regard to equation (F.2).

What concerns the momentum matrix elements,  $\langle \phi_{\mathbf{k}+\mathbf{G}} | -i\nabla | \phi_{\mathbf{k}+\mathbf{G}'} \rangle$ , the inner product is split into contributions from the muffin-tin spheres and the interstitial region, the latter being

$$\langle \phi_{\mathbf{k}+\mathbf{G}} | \nabla | \phi_{\mathbf{k}+\mathbf{G}'} \rangle_{\text{Interstitial}} = i(\mathbf{k} + \mathbf{G}')\Theta(\mathbf{G} - \mathbf{G}'). \quad (\text{F.9})$$

The contribution from muffin-tin spheres are evaluated analogously to equation (F.5).

At last, the element of the LAPW-lo and lo-LAPW blocks in equation (4) are expressed as

$$\langle \phi_{\mathbf{k}+\mathbf{G}} | \hat{H}(t) | \phi_{\gamma'} \rangle = \sum_{\nu} (\mathcal{A}_{\nu\mathbf{G}}^{\alpha\mathbf{k}})^* h_{\nu\gamma'}(t) + \frac{\mathbf{A}^2(t)}{2c^2} [S_{\mathbf{k}}]_{\mathbf{G}\gamma'} - \frac{i}{c} \mathbf{A}(t) \cdot \langle \phi_{\mathbf{k}+\mathbf{G}} | \nabla | \phi_{\gamma'} \rangle, \quad (\text{F.10})$$

where the overlap matrix is calculated as

$$\langle \phi_{\mathbf{k}+\mathbf{G}} | \phi_{\gamma'} \rangle = \sum_{\nu} (\mathcal{A}_{\nu\mathbf{G}}^{\alpha\mathbf{k}})^* s_{\nu\gamma'}^{\alpha}, \quad (\text{F.11})$$

and  $\langle \phi_{\mathbf{k}+\mathbf{G}} | \nabla | \phi_{\gamma'} \rangle$  is obtained like in the lo–lo case.

Exploiting hermiticity, we obtain  $\langle \phi_{\gamma} | \hat{H}(t) | \phi_{\mathbf{k}+\mathbf{G}'} \rangle$ ,  $\langle \phi_{\gamma} | \phi_{\mathbf{k}+\mathbf{G}'} \rangle$  and  $\langle \phi_{\gamma} | \nabla | \phi_{\mathbf{k}+\mathbf{G}'} \rangle$ .

## ORCID iDs

Ronaldo Rodrigues Pela  <https://orcid.org/0000-0002-2413-7023>

Claudia Draxl  <https://orcid.org/0000-0003-3523-6657>

## References

- [1] Runge E and Gross E K U 1984 *Phys. Rev. Lett.* **52** 997–1000
- [2] Botti S, Schindlmayr A, Sole R D and Reining L 2007 *Rep. Prog. Phys.* **70** 357
- [3] Andrade X *et al* 2012 *J. Phys.: Condens. Matter.* **24** 233202
- [4] Jornet-Somoza J, Alberdi-Rodriguez J, Milne B F, Andrade X, Marques M A L, Nogueira F, Oliveira M J T, Stewart J J P and Rubio A 2015 *Phys. Chem. Chem. Phys.* **17** 26599–606
- [5] Maitra N T 2016 *J. Chem. Phys.* **144** 220901
- [6] Kolesov G, Grånäs O, Hoyt R, Vinichenko D and Kaxiras E 2016 *J. Chem. Theory Comput.* **12** 466–76
- [7] Morzan U N, Ramírez F F, Oviedo M B, Sánchez C G, Scherlis D A and Lebrero M C G 2014 *J. Chem. Phys.* **140** 164105
- [8] Bende A 2015 Chapter three—modeling laser-induced molecule excitations using real-time, time-dependent density functional theory *Annual Reports in Computational Chemistry* 11 (*Annual Reports in Computational Chemistry* vol 11) ed D A Dixon (Amsterdam: Elsevier) pp 103–46
- [9] Yabana K, Sugiyama T, Shinohara Y, Otobe T and Bertsch G F 2012 *Phys. Rev. B* **85** 045134
- [10] Meng S and Kaxiras E 2008 *J. Chem. Phys.* **129** 054110
- [11] Sato S A, Taniguchi Y, Shinohara Y and Yabana K 2015 *J. Chem. Phys.* **143** 224116
- [12] Lian C, Guan M, Hu S, Zhang J and Meng S 2018 *Adv. Theor. Simul.* **1** 1800055
- [13] Ojanperä A, Havu V, Lehtovaara L and Puska M 2012 *J. Chem. Phys.* **136** 144103
- [14] Yamada A and Yabana K 2019 *Phys. Rev. B* **99** 245103
- [15] Sato S, Hübener H, De Giovannini U and Rubio A 2018 *Appl. Sci.* **8** 1777
- [16] Miyamoto Y, Zhang H, Miyazaki T and Rubio A 2015 *Phys. Rev. Lett.* **114** 116102

- [17] Maitra N T 2017 *J. Phys.: Condens. Matter.* **29** 423001
- [18] Refaely-Abramson S, Jain M, Sharifzadeh S, Neaton J B and Kronik L 2015 *Phys. Rev. B* **92** 081204
- [19] Pemmaraju C D 2019 *Comput. Condens. Matter* **18** e00348
- [20] Imamura Y, Suzuki K, Iizuka T and Nakai H 2015 *Chem. Phys. Lett.* **618** 30–6
- [21] Rigamonti S, Botti S, Veniard V, Draxl C, Reining L and Sottile F 2015 *Phys. Rev. Lett.* **114** 146402
- [22] Lejaeghere K *et al* 2016 *Science* **351** aad3000
- [23] Gulans A, Kozhevnikov A and Draxl C 2018 *Phys. Rev. B* **97** 161105
- [24] The exciting code <http://exciting-code.org/>
- [25] Gulans A, Kontur S, Meisenbichler C, Nabok D, Pavone P, Rigamonti S, Sagmeister S, Werner U and Draxl C 2014 *J. Phys.: Condens. Matter.* **26** 363202
- [26] Tancogne-Dejean N *et al* 2020 *J. Chem. Phys.* **152** 124119
- [27] Bertsch G F, Iwata J-I, Rubio A and Yabana K 2000 *Phys. Rev. B* **62** 7998–8002
- [28] Yabana K, Nakatsukasa T, Iwata J-I and Bertsch G F 2006 *Phys. Status Solidi b* **243** 1121–38
- [29] Pemmaraju C D, Vila F D, Kas J J, Sato S A, Rehr J J, Yabana K and Prendergast D 2018 *Comput. Phys. Commun.* **226** 30–8
- [30] Marques M A L, Ullrich C A, Nogueira F, Rubio A, Burke K and Gross E K U (ed) 2006 *Time-Dependent Density Functional Theory (Lecture Notes in Physics vol 706)* (Berlin: Springer)
- [31] Marques M A L, Maitra N T, Nogueira F M S, Gross E K U and Rubio A (ed) 2012 *Fundamentals of Time-Dependent Density Functional Theory (Lecture Notes in Physics vol 837)* (Berlin: Springer)
- [32] Vorwerk C, Aurich B, Cocchi C and Draxl C 2019 *Electron. Struct.* **1** 037001
- [33] Ambrosch-Draxl C and Sofo J O 2006 *Comput. Phys. Commun.* **175** 1–14
- [34] Castro A, Marques M A L and Rubio A 2004 *J. Chem. Phys.* **121** 3425–33
- [35] Gómez Pueyo A, Marques M A L, Rubio A and Castro A 2018 *J. Chem. Theory Comput.* **14** 3040–52
- [36] Dewhurst J K, Krieger K, Sharma S and Gross E K U 2016 *Comput. Phys. Commun.* **209** 92–5
- [37] Griffiths D J 2013 *Introduction to Electrodynamics* (Harlow: Pearson Education)
- [38] Temnov V V, Sokolowski-Tinten K, Zhou P, El-Khamhawy A and von der Linde D 2006 *Phys. Rev. Lett.* **97** 237403
- [39] Sato S A, Yabana K, Shinohara Y, Otobe T and Bertsch G F 2014 *Phys. Rev. B* **89** 064304
- [40] Sokolowski-Tinten K and von der Linde D 2000 *Phys. Rev. B* **61** 2643–50
- [41] Zheng Q, Chu W, Zhao C, Zhang L, Guo H, Wang Y, Jiang X and Zhao J 2019 *Wiley Interdiscip. Rev.: Comput. Mol. Sci.* **9** e1411
- [42] Li Y, He S, Russakoff A and Varga K 2016 *Phys. Rev. E* **94** 023314
- [43] Otobe T, Yamagiwa M, Iwata J-I, Yabana K, Nakatsukasa T and Bertsch G F 2008 *Phys. Rev. B* **77** 165104
- [44] Otobe T, Yabana K and Iwata J-I 2009 *J. Phys.: Condens. Matter.* **21** 064224
- [45] Draxl C and Scheffler M 2019 *J. Phys. Mater.* **2** 036001
- [46] Rodrigues Pela R and Draxl C Nomad Repository 2021 dataset: rttddft-exciting <https://dx.doi.org/10.17172/NOMAD/2021.01.20-1>